

FOURTH EUROPEAN ROTORCRAFT AND POWERED LIFT AIRCRAFT FORUM

Paper No. 21

AN EXPERIMENTAL STUDY OF COUPLED ROTOR-BODY
AEROMECHANICAL INSTABILITY OF HINGELESS ROTORS
IN HOVER

WILLIAM G. BOUSMAN AND DEWEY H. HODGES

Aeromechanics Laboratory
U.S. Army Research and Technology Laboratories (AVRADCOM)
Ames Research Center
Moffett Field, California 94035, U.S.A.

September 13-15, 1978

STRESA - ITALY

Associazione Italiana di Aeronautica ed Astronautica
Associazione Industrie Aerospaziali

AN EXPERIMENTAL STUDY OF COUPLED ROTOR-BODY
AEROMECHANICAL INSTABILITY OF HINGELESS ROTORS

IN HOVER

William G. Bousman and Dewey H. Hodges
Aeromechanics Laboratory
U.S. Army Research and Technology Laboratories (AVRADCOM)
Ames Research Center
Moffett Field, California 94035, U.S.A.

SUMMARY

A 1.62-m diameter, three-bladed rotor model was tested in hover to examine aeromechanical stability of coupled rotor-body systems. Excellent modal frequency data and good lead-lag regressing mode damping data were obtained over a wide range of rotor speeds. Damping data for the body modes were not satisfactory due to nonlinear damping of the gimbal ball bearings. Simulated vacuum testing was performed with circular cross section blades made of tantalum, which resulted in a Lock number 0.2% of the aerodynamic value. The experimental data were compared with theoretical predictions, and the overall agreement was very good.

1. Introduction

Soft inplane hingeless rotor helicopters are susceptible to aeromechanical instabilities in hover and on the ground, commonly known as air and ground resonance. Instabilities of this type occur when the rotor lead-lag regressing mode and a body pitch or roll mode become proximate or coalesce. The classical condition of ground resonance as analyzed by Coleman and Feingold (Ref. 1) for articulated rotors is a purely mechanical instability, and as such represents a restricted class of problems where coupling between the rotor and body can be simply represented and the effects of aerodynamics ignored. For the hingeless rotor helicopter, however, coupling between the rotor and body is quite complex, and the rotor aerodynamics significantly affect system stability. A number of mathematical models of aeromechanical stability have been developed (Refs. 2-4) and these have been used in the design of helicopters with soft inplane rotors. In addition, Boeing Vertol has used small-scale development models to investigate parameters affecting aeromechanical stability (Refs. 5-6) and thereby gained confidence in their analyses. Despite these efforts, a comprehensive understanding of aeromechanical stability has not been achieved.

The complexity of coupled rotor-body systems suggests that a valid mathematical model is required in the development of any hingeless rotor helicopter. Although useful in the design and development of a rotorcraft, such a model may be overly cumbersome for use as a general research tool. In particular, if a broad, fundamental understanding of coupled rotor-body stability is desired, then a simplified analytical model is required that can adequately represent the essential features of the coupled rotor-body problem, but is flexible enough to allow wide parameter variation. This is the rationale used by Ormiston in developing the theoretical model discussed in Ref. 7. The same distinction exists between an experimental model used in the development of a new rotorcraft design, and one designed purely as a research tool (e.g., Ref. 8).

The present experiment has been designed to use a relatively simple experimental model in a manner analogous to the theoretical model of Ref. 7. The objectives of the experiment are: (1) to obtain a set of data that can be used to validate simple theoretical models of coupled rotor-body systems, (2) to explore the character of aeromechanical stability of hingeless rotor helicopters, and (3) to evaluate test techniques suitable for rotor-body stability testing.

The model used in these experiments simulates a hingeless rotor by using a rigid blade with a spring-restrained root hinge in the manner of Ref. 7. However, the hinge location for the experimental model is offset from the rotor center, and as hinge offset is not included in the theoretical model of Ref. 7, the analysis of Ref. 9 is used in the comparison of theory and experiment. The theoretical model of Ref. 9, although developed for the purpose of examining the aeroelastic stability of bearingless rotors, is also capable of treating the present experimental model with its high torsional rigidity.

The paper contains, first, a discussion of the theoretical model, and then describes the design of the experiment, including validation process requirements, model characteristics, and test procedures. Comparisons are then made between theory and experiment, and conclusions are offered.

2. Analytical Model

In this section, the analytical model used to represent the experimental model is described. The theory is actually based on a more general analytical model developed for bearingless rotor helicopters and described in Refs. 9 and 10. This discussion includes only elements of the analytical model actually used in the study of air and ground resonance stability of the experimental model.

The dynamical system consists of two parts, the body and the rotor. The body is assumed to be a rigid body mounted on spring- and damper-restrained hinges in the pitch and roll directions. Translations of the body, although present in the analysis (Ref. 10), are ignored for correlation with the experimental data.

A schematic of the body is shown in Fig. 1. Contributions of the hub and mast are included in the mass and inertia properties of the body. The total mass of the body is m_f and the moments of inertia for the mass center of the body are I_x and I_y , respectively, for the X and Y directions. The aircraft reference center, shown in Fig. 1, is a distance z above the body mass center and a distance h below the hub center. In studying air resonance and ground resonance, in hover and on the ground, respectively, vertical translation and yaw rotation of the body are insignificant. In this paper, body roll ϕ_x and body pitch ϕ_y degrees of freedom are included. Body spring stiffness restrains the ϕ_x and ϕ_y motion.

The rotor blades are attached to the hub and rotate at constant angular velocity Ω . The blade has a built-in pitch angle offset relative to the flexbeam θ_b . A schematic of one rotor blade is shown in Fig. 2. The analysis has been developed to treat different pitch-control configurations; however, in the present case the blade is considered to be unrestrained by any form of control system (Fig. 2). In the analysis the flexure or strap is treated as a single uniform beam segment.

3. Theoretical Analysis

A complete derivation of the equations of motion used in this analysis is beyond the scope of this paper; the derivation is given in Ref. 10. The analysis is based on the set of generalized forces due to inertia, gravity, body springs (when the aircraft is in ground contact), quasi-steady aerodynamics, and the flexbeam structure. All these generalized forces (except those due to flexbeam structural loads) can be written exactly, within these assumptions for the above analytical model, and analytically linearized about equilibrium. The flexbeam equilibrium deflections can be calculated through a nonlinear numerical iteration process, and the flexbeam structural loads for small perturbation deflections can be determined through numerical perturbation of the equilibrium solution. These steps lead to a system of linear, constant-coefficient, homogeneous, ordinary differential equations.

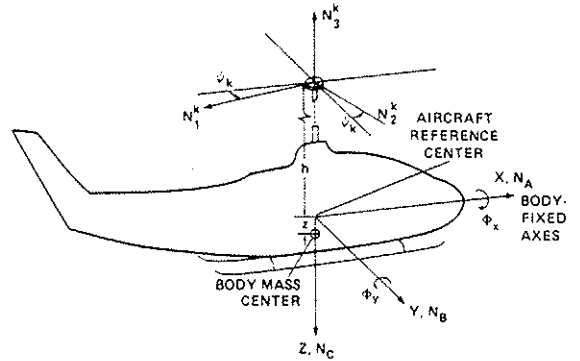


Fig. 1. Rotorcraft body model.

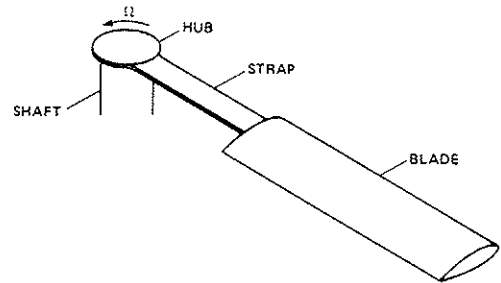


Fig. 2. Schematic of blade geometry.

3.1 Generalized Forces

In addition to the rigid-body degrees of freedom ϕ_x, ϕ_y , described above, the six degrees of freedom of the k th blade in the rotating system may be expressed as: (1) three translations of the blade root corresponding to the n_1^k, n_2^k, n_3^k axis system, u_k, v_k, w_k , respectively; and (2) three rotations $\zeta_k, \beta_k, \theta_k$, lead, flap, and pitch angles, respectively, of the blade (beginning with ζ_k about the n_3^k axis, β_k about the axis $\cos \zeta_k n_2^k - \sin \zeta_k n_1^k$, and θ_k about n_x^k axis). Such a sequence is noted only for the purpose of definition; obviously, the sequence of angles will not affect the solution of the equations of motion.

Exact expressions for the generalized forces due to inertia, gravity, body springs, the pitch-control systems, and quasi-steady airloads are derived in Ref. 10. The total forces acting along the blade may be resolved into a force and moment acting at the tip of the k th flexbeam. These are exactly balanced by the structural loads that the k th flexbeam exerts on the k th blade. This is true because all external loads acting along the flexbeam are neglected. All of the loads except the structural loads of the flexbeam can be expressed in closed form. A numerical scheme that solves the equilibrium deflections is described in the next section, treating the flexbeam structural loads implicitly.

3.2 Flexbeam Equilibrium Deflections

The force vector F_k , representing forces that the k th blade exerts on the k th flexbeam, and the moment vector M_k , representing the

moments that the kth blade exerts on the kth flexbeam, have steady and unsteady components:

$$\begin{aligned} F_k &= F + \tilde{F}_k(t) \\ M_k &= M + \tilde{M}_k(t) \end{aligned} \tag{1}$$

Quantities without subscripts are steady components and the tilde quantities are unsteady components. Similarly,

$$\begin{aligned} u_k &= u + \tilde{u}_k(t) \\ v_k &= v + \tilde{v}_k(t) \\ w_k &= w + \tilde{w}_k(t) \\ \zeta_k &= \zeta + \tilde{\zeta}_k(t) \\ \beta_k &= \beta + \tilde{\beta}_k(t) \\ \theta_k &= \theta + \tilde{\theta}_k(t) \end{aligned} \tag{2}$$

The steady components F and M possess geometric nonlinearity in $u, v, w, \zeta, \beta, \theta$. The unsteady components \tilde{F}_k and \tilde{M}_k may be analytically linearized in the following quantities and their first and second derivatives: $\tilde{u}_k, \tilde{v}_k, \tilde{w}_k, \tilde{\zeta}_k, \tilde{\beta}_k, \tilde{\theta}_k, \phi_x, \phi_y$.

Consider only the steady part of the solution. If $u, v, w, \zeta, \beta, \theta$ were known (the deflections of the blade and tip of the flexbeam), then F and M would be determined. These deflections are not known, however. If the forces and moments at the root of the flexbeam F_R, M_R were known, the geometrically exact expressions for the curvature-slope-deflection relations could be numerically integrated along the flexbeam to obtain the correct tip deflections. Thus, what we have is a type of two-point boundary value problem. The expressions relating the tip deflections to tip forces and moments are known. The relation between root forces and moments and tip deflections is determined through numerical integration.

A workable, accurate scheme for the solution of this problem is given in the following seven steps: (1) assume a set of flexbeam tip deflections $u_t, v_t, w_t, \zeta_t, \beta_t, \theta_t$, (2) calculate the force and moment F and M based on the assumed deflections, (3) transfer the force and moment F and M to the equivalent root force and moment F_R and M_R using the assumed tip deflections, (4) evaluate the tension force and bending and torsion moments for a generic point along the flexbeam in terms of the deflections $u, v, w, \zeta, \beta, \theta$, each a function of the distance along the deformed flexbeam, (5) using moment-curvature relations, numerically integrate the geometrically exact expressions relating bending and torsion curvatures to slopes and deflections (Ref. 10), (6) compare the assumed tip deflections $u_t, v_t, w_t, \zeta_t, \beta_t, \theta_t$ with the tip deflections $u, v, w, \zeta, \beta, \theta$ of step (5), (7) place steps (1) through (6) in an

optimization scheme to minimize

$$\mathcal{F} = (u - u_t)^2 + (v - v_t)^2 + (w - w_t)^2 + (\zeta - \zeta_t)^2 + (\beta - \beta_t)^2 + (\theta - \theta_t)^2 \quad (3)$$

Naturally, the minimum $\mathcal{F} = 0$ is the exact solution to the equilibrium position of the rotor blades. This minimum can be found by use of a non-linear least squares algorithm.

3.3 Perturbation Flexbeam Structural Loads

In addition to the equilibrium solution the perturbation forces and moments that the flexbeam exerts in response to perturbation deflections must be determined. This is done by cyclically perturbing the equilibrium force and moment components in the directions of $u, v, w, \zeta, \beta, \theta$ and looking at the new deflections. Symbolically, this is expressed as

$$\begin{pmatrix} \tilde{u}_k \\ \tilde{v}_k \\ \tilde{w}_k \\ \tilde{\zeta}_k \\ \tilde{\beta}_k \\ \tilde{\theta}_k \end{pmatrix} = [F] \begin{pmatrix} \tilde{F}_{u_k} \\ \tilde{F}_{v_k} \\ \tilde{F}_{w_k} \\ \tilde{M}_{\zeta_k} \\ \tilde{M}_{\beta_k} \\ \tilde{M}_{\theta_k} \end{pmatrix} \quad (4)$$

where $[F]$ is a 6 x 6 matrix, identical for all k , the elements of which are

$$F_{ij} = \frac{(\text{ith deflection due to jth perturbed load}) - \text{ith equilibrium deflection}}{\epsilon} \quad (5)$$

and ϵ is the amount the loads are perturbed. The matrix elements are symmetric for infinitesimal ϵ . Numerically, however, ϵ cannot be any smaller than the square root of the relative error of the deflections. This will depend on the error criterion in the optimization algorithm. On the other hand, an ϵ that is too large will produce slight nonsymmetry in $[F]$ due to geometric nonlinearity. The force and moment response of the flexbeam to small perturbations of the deflection may be obtained from Eq. (4) by simply inverting $[F]$. The resulting matrix $[F^{-1}]$ is the structural stiffness matrix for the flexbeam. To complete the system equations of motion, this matrix may now be combined with the linearized, unsteady perturbation forces and moments produced by the pitch-control system, inertia, gravity, quasi-steady aerodynamics, and the body springs.

3.4 Linearized Perturbation Equations

When all of the generalized forces associated with both blade and body degrees of freedom are linearized in $\tilde{u}_k, \tilde{v}_k, \tilde{w}_k, \tilde{\zeta}_k, \tilde{\beta}_k, \tilde{\theta}_k, \phi_x, \phi_y$, and in their first and second time derivatives, there are many terms with coefficients $\cos \psi_k$ and $\sin \psi_k$. In hover, all of these may be removed

by the multiblade coordinate transformation (Ref. 11). The details of applying this transformation to the present problem are given in Ref. 10. Only the rotor cyclic modes are coupled to the ϕ_x, ϕ_y body motion, and hence, the collective and differential collective modes are not included in the present analysis. The two cyclic modes for six degrees of freedom each, plus the two body modes, yields fourteen degrees of freedom $\bar{u}_c, \bar{u}_s, \bar{v}_c, \bar{v}_s, \bar{w}_c, \bar{w}_s, \bar{\zeta}_c, \bar{\zeta}_s, \bar{\beta}_c, \bar{\beta}_s, \bar{\theta}_c, \bar{\theta}_s, \phi_x, \phi_y$, where

$$\bar{u}_c = \frac{2}{b} \sum_{k=1}^b \bar{u}_k \cos \psi_k \quad (6)$$

$$\bar{u}_s = \frac{2}{b} \sum_{k=1}^b \bar{u}_k \sin \psi_k$$

$$\vdots$$

and

$$\bar{F}_{u_c} = \frac{2}{b} \sum_{k=1}^b \bar{F}_{u_k} \cos \psi_k \quad (7)$$

$$\bar{F}_{u_s} = \frac{2}{b} \sum_{k=1}^b \bar{F}_{u_k} \sin \psi_k$$

$$\vdots$$

These 14 resulting linear ordinary differential equations with constant coefficients can be formed into a matrix equation

$$[A]\{\dot{x}\} + [B]\{\dot{x}\} + [C]\{x\} = 0 \quad (8)$$

where $[A]$, $[B]$, and $[C]$ contain elements that depend on the system parameters and blade equilibrium deflections $u, v, w, \zeta, \beta, \theta$. These matrices contain no small angle assumptions or geometric approximations. Equation (8) is solved as a conventional eigenvalue problem.

4. Mathematical Model Validation

A primary objective of the experiment was to provide data suitable for use in validating mathematical models of coupled rotor-body systems. To be successful, the validation process must meet three requirements: (1) the experimental model must closely simulate the theoretical model; (2) the parameter variation must be sufficiently extensive to test the limitations of the theory; and (3) the bases of comparison between theory and experiment must be valid.

The requirement that the experimental model simulate the analytical model is necessary to insure that differences between the theoretical predictions and experimental measurements reflect limitations of the theory and not the experimental modeling process. As an example, the simplified theoretical model of Ref. 7 assumes that the rotor blades are hinged at the hub centerline and that their stiffness is due to a hinge-mounted spring. In the design of an experimental model it is difficult to place the hinge centerline at the rotor center. Thus, in any comparison of theory and experiment, there will be an effect due to hinge offset that is in the experimental data but not in the theory. The resulting ambiguity is that there is no way to know whether a difference that occurs is due solely to hinge offset, or whether there is an additional source of error.

There are other difficulties that occur in designing an experimental model to match a simplified mathematical model. Of these, joints and bearings present one of the more troublesome problems. Any loose joint, and many kinds of bearings, introduce friction or viscous damping and slop. Particularly at model scale, nonlinearities or excessive damping can drastically affect system damping and must be avoided. A second problem is that of extraneous system modes. The simplified theoretical model may assume that the blade is rigid or that body motion is constrained purely to pitch and roll. The experimental model, in fact, will have numerous higher modes, and the model designer's problem is to insure that these modes do not couple with the primary modes of interest. In emphasizing the necessity of the experiment matching the theory, it is also necessary to point out that the simplified theory must provide an adequate representation of potential helicopter designs, or the entire exercise loses its value.

The second requirement in the validation process is the need to provide for extensive parameter variation in the experimental design. Every parameter that is of significance in the theoretical model defines a dimension in an n-dimensional space that defines the model region of applicability. To validate the theory over the entire n-dimensional space would be difficult and would undoubtedly be a waste of time. However, it is desirable to select the more significant parameters and provide a sufficient range of variation to determine the limitations of the theory. Clearly, comparing theory and experiment for one or two points is of little value.

The third requirement is that the bases of comparison must be valid. In investigating the aeromechanical stability of a hingeless rotor helicopter, the behavior of the least damped mode is of the greatest importance; but there are a number of bases of comparison that may be used in the validation process, and some may be more useful than others. A hierarchy of these bases can be devised, the lowest basis of which is the easiest to obtain but provides the least confidence in the theory, while the highest basis represents the most difficult experimental problem but provides the greatest confidence in the theory. For aeromechanical stability tests, an appropriate hierarchy starts with frequency measurements of a single mode, frequencies of all significant modes, stability boundaries, modal damping of a single mode and then all significant modes, and finally, mode shape measurements representing the most difficult problem. In selecting appropriate bases for an experiment, it may be necessary to strike a balance between the level of confidence that is needed and the difficulty of the experimental problem.

5. Experimental Model

Experimental data were obtained with a 1.62-m diameter, three-bladed model rotor as shown in Fig. 3. The electrically powered model is mounted on a gimbal frame that allows pitch and roll freedom, and the various modes of the system are excited by an electromagnetic shaker that is attached to the body through a linkage and pneumatic clamp.

The rotor blades were designed to be very stiff, and most of the blade flexibility is concentrated in root flexures as shown in an exploded view in Fig. 4. The root flexures are designed so that the lead-lag and flapping flexibility are in separate flexures. By folding the structure back on itself, the spanwise locations of the flexures are made coincident. The design of the flexures is such that the torsional stiffness is very

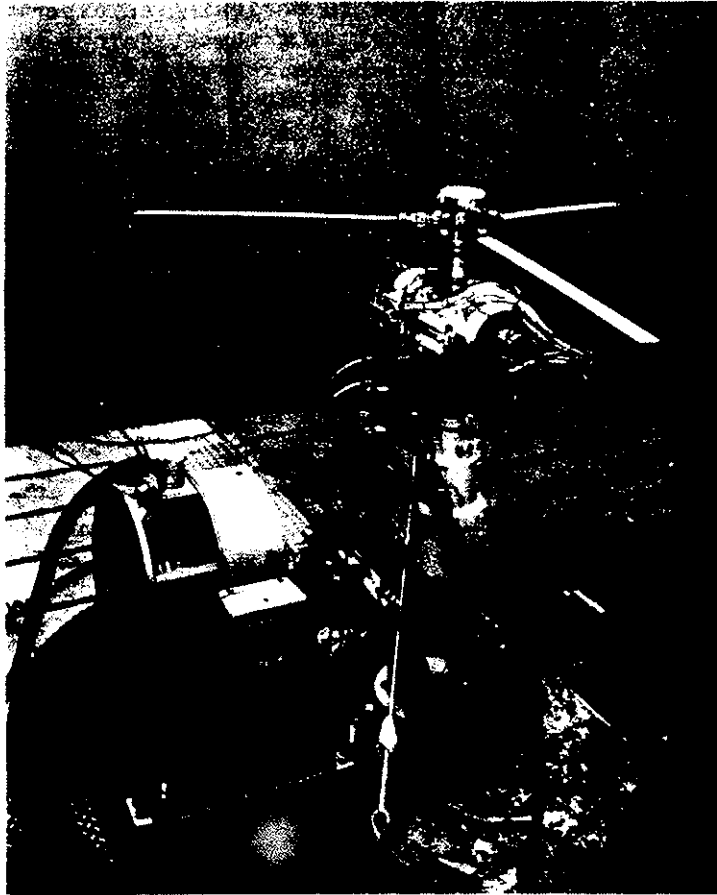


Fig. 3. 1.62-m diameter rotor model.

high; at 1000 rpm the blade nondimensional torsion frequency is greater than 20/rev. By designing the blades to be very stiff, and concentrating the major portion of flexibility in the root flexures, the model design approximates a rotor blade with only one flap and one lead-lag degree of freedom. This design provides a good approximation of the theoretical model that assumes all blade flexibility to be concentrated in a flexible element at the blade root. However, some blade flexibility is outboard of the root flexures (Ref. 12), and to this degree the model design differs from the theory. The root flexures are strain-gaged to provide measurements of flap and lead-lag bending moments and torsional moments for each blade. Blade pitch angle changes are made outboard of the flexures.

The blades and root flexures are bolted to a hub that is mounted on a static mast, as shown in the schematic of Fig. 5. The static mast is bolted to the body, which is supported on either end by ball bearings. These ball bearings provide the body with roll freedom and are supported in a gimbal frame that is mounted to the yoke by a second set of ball bearings that provide pitch freedom. The yoke is the upper part of the stand, which provides a rigid support for the model.

The model is excited about the roll axis by an electromagnetic shaker that is connected to the body with a pneumatic clamp. The shaker may be used to oscillate the body at a specific frequency or to provide an input deflection in roll. By opening the pneumatic clamp, the body is then unconstrained and measurements are made of the transient decay of the

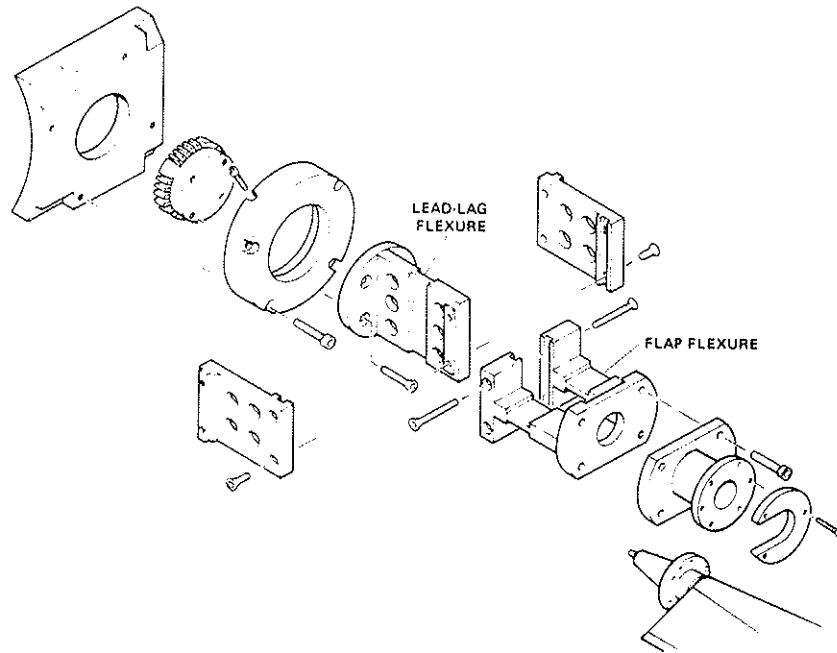


Fig. 4. Exploded view of blade root flexures.

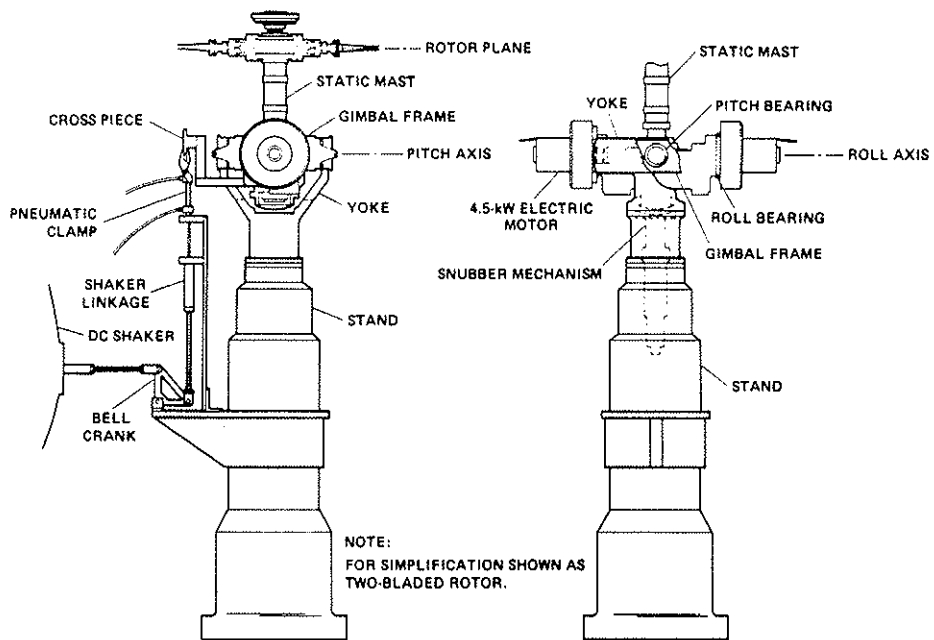


Fig. 5. Schematic drawing of rotor model and test stand.

modes that have been excited. For unstable conditions, a snubber mechanism within the stand may be actuated by the operator, or the snubber will automatically lock out body motions in the event that blade bending moments become excessive.

Body stiffness is provided by cantilever-beam springs, one in roll and two in pitch. Each spring includes a slider that allows the working

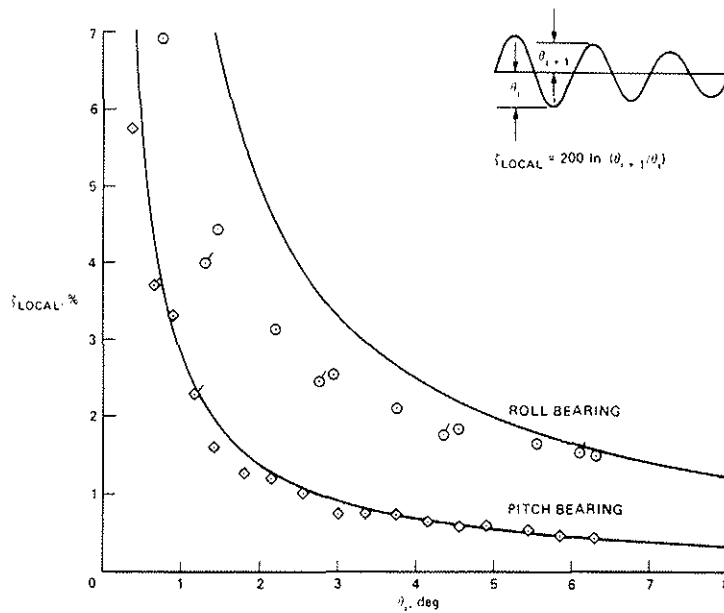


Fig. 6. Local damping coefficient of gimbal pitch and roll bearings.

length of the beam spring to be changed to adjust the body stiffness, and hence, frequency. The range of body frequencies is from about 2 to 20 Hz. This design provides a good match of the theoretical model, in that the body motions are constrained to purely pitch and roll motions, at least at the lower body frequencies. At higher frequencies, however, the motion of the body will include some translational motions due to flexibility in the static mast.

Body damping is supplied by damping in the gimbal ball bearings. Unfortunately, this damping is nonlinear with amplitude as shown in Fig. 6, where a local damping coefficient is defined based upon the log decrement per half cycle. The increase in damping with a decrease in amplitude is typical of Coulomb, or dry friction. If it is hypothesized that the source of the dry friction is the rubbing between the balls and the cage of the ball bearing, then the damping moment will be proportional to (1) the number of balls in the bearing that are restrained by the cage, (2) the friction force between ball and cage, and (3) the radius at which the friction force acts. A solution for the nonlinear equation describing a single degree of freedom system (Ref. 13) is shown in Fig. 6, where the friction force per ball is selected to match the experimental results at $\theta_1 = 6^\circ$ for the pitch bearing. The presence of nonlinear damping in the experimental model is a deficiency that would be expected to cause some difficulty in correlating the results of theory and experiment.

Measurements of body motion are made with two accelerometers mounted just below the hub on the static mast and film potentiometer strips on the gimbal frame. The bending moment signals on the rotor are routed through a set of slip rings at the base of the rotor drive shaft; these are combined with the body measurements, 1/rev and 60/rev signals, lubricating oil lines, and cooling water lines and routed off the model in a manner to minimize their interference with body motions. Additional details relative to the model design and instrumentation are contained in Ref. 14.

6. Simulated Vacuum Tests

The stability of coupled rotor-body motions is strongly affected by the blade aerodynamics. In the validation of a theoretical model, it would be desirable to test a model in a vacuum to observe the effect of inertial and structural properties without aerodynamics. However, vacuum testing is a difficult experimental problem. A partial solution is to simulate a vacuum by testing at a reduced Lock number. If the definition of Lock number is modified to include the effect of the profile drag coefficient

$$\gamma_d = \frac{\rho a c R^4}{I} \left(1 + \frac{c_{d_o}}{a} \right) \quad (9)$$

The Lock number may be reduced by substituting a blade of circular cross section where the lift curve slope is zero. If the circular cross section blade is assumed to have a uniform density, the Lock number becomes

$$\gamma_d = \frac{12 \rho c d_o}{\pi} \left(\frac{R}{\rho_d c} \right) \quad (10)$$

and it is seen that the Lock number is proportional to the radius and inversely proportional to the density of the rod and blade chord. If the constraint is added that blade flap inertia must not change from the aerodynamic blade flap inertia, then:

$$\rho_d c^2 R^3 = \frac{12I}{\pi} = \text{constant} \quad (11)$$

From these relations it appears that material density and blade chord should be increased, and blade radius reduced. It is important to note, however, that other dynamic properties of the rotor will be affected by these changes; e.g., dimensionless hinge offset increases proportionally to $1/R$, while rotor mass increases as $1/R^2$. Large decreases in rotor radius will therefore cause a large hinge offset effect, and reduce the body frequencies due to the effect of the increased rotor mass. In addition, the flexibility of the circular cross section blade cannot be easily matched to the aerodynamic blade flexibility. In the present case, this latter point is unimportant as the theoretical model assumes that the blade is rigid.

The configuration selected for this experiment is a reduction in blade radius from 81 cm to 38 cm and a selection of tantalum for the blade material. Tantalum has a density greater than lead, but has strength and stiffness characteristics similar to steel. The Lock number for this configuration is reduced to 0.2% of the aerodynamic blade value. A picture of the model with the tantalum blades installed is shown in Fig. 7.

7. Modal Measurement Considerations

The essential problem of the experiment is to understand the behavior of the modes that affect the aeromechanical stability of the coupled rotor-body system. An introduction to the behavior of these modes and how to measure their characteristics can be obtained by examining the case of a rotor mounted on a rigid hub, where each blade has a flap and a lead-lag degree of freedom. For a three-bladed rotor, then, the

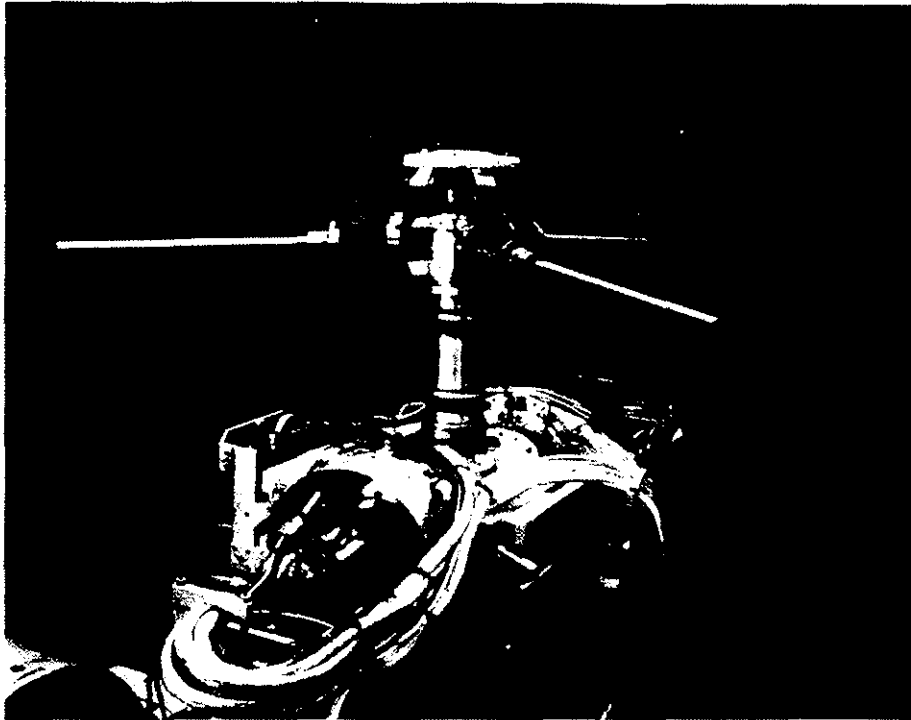


Fig. 7. Rotor model with tantalum stub blades installed.

individual blade modes will combine to form six rotor modes: collective flap, collective lead-lag, two cyclic flap, and two cyclic lead-lag modes. The two collective modes will not couple with body pitch and roll motions in hover and may be safely ignored. The frequencies of the cyclic modes will appear in the fixed system at sum and difference frequencies between rotor speed and the individual blade natural frequencies as shown in Fig. 8 (where the individual blade natural frequencies in the rotating system are shown as dashed lines). The higher frequency modes that are based on the sum are referred to as progressing modes, while the lower frequency modes based on the difference are the regressing modes.

For rotor speeds below the resonance of rotor speed and the lead-lag natural frequency ($\Omega = \omega_{\zeta}$), rotors may be characterized as stiff inplane. Rotor speeds beyond the resonance describe soft inplane configurations. It is in this latter regime that the coupled rotor-body instabilities, ground and air resonance, normally occur. The experimental problem, then, is to select body modes with frequencies in the range of the lead-lag regressing mode and observe the behavior of the coupled rotor-body system.

The frequency and damping of the rotor regressing modes and the body pitch and roll modes provide an accurate description of coupled rotor-body behavior, and are suitable bases of comparison between theory and experiment. To observe these modes directly, however, is difficult, as neither the rotor regressing nor the body modes correspond directly to a physical coordinate. The body pitch mode includes pitch motion, to be sure, but also includes roll motion and rotor flapping. The body roll mode behaves similarly, while the flap regressing mode is made up of not only flapping, but both body motions as well. Moreover, neither the flap nor the lead-lag regressing mode can be identified from individual blade bending moment signals. To observe these modes it is necessary to transform the individual blade coordinates to multiblade coordinates (Ref. 11).

The multiblade coordinates for a three-bladed rotor include a collective coordinate and two cyclic coordinates for both flap and lead-lag degrees of freedom. For a hovering rotor, the flap and lead-lag collective coordinates make up the flap and lead-lag collective modes, respectively. But the lead-lag regressing mode, for example, includes both cyclic lead-lag coordinates, as does the lead-lag progressing mode. Thus, measurements of either cyclic lead-lag coordinate will show the presence of both modes. To observe the lead-lag regressing mode directly requires a narrow bandpass filter to separate the regressing and progressing modes.

The frequency and damping of the modes of interest are obtained by exciting the mode, and measuring the frequency and damping from the transient decay. In the case of the lead-lag regressing mode, the model was

oscillated in roll at the regressing mode frequency until the blade motions were sufficiently large, at which point the excitation was cut off and the pneumatic clamp that connects the model to the shaker was opened so that the mode could decay without restraint due to the shaker. The flap regressing (in the simulated vacuum case) and the body roll mode could not be excited at their modal frequencies without causing excessive loads due to lead-lag response. This is probably an inherent limitation of the transient decay method whenever there is a significant difference in damping between nearby modes. However, both flap regressing and body roll modes could be excited by deflecting the model in roll and quickly releasing it. Responses of the two modes were then separated using a narrow bandpass filter. The body pitch mode was excited to the extent it participated in motion about the roll axis, and by gyroscopic coupling.

Transient decay records were analyzed for modal frequency using both an online spectrum analyzer, and by playing the signals recorded on analog tape back through a tracking filter. Modal damping was determined from analog tape records using the log RMS amplitude of the tracking filter as described in Ref. 15.

8. Comparison of Theory and Experiment

The configurations tested that will be discussed here are: (1) tantalum stub blades with roll freedom, (2) tantalum stub blades with both pitch and roll freedom, and (3) aerodynamic blades with pitch and roll freedom. Other configurations tested and the comparison of theory and experiment may be found in Ref. 14. For each configuration tested, the primary parameter variation used was rotor speed. By varying rotor speed from approximately 250 to 1000 rpm, rotor configurations were simulated from stiff inplane ($\omega_\zeta/\Omega \sim 1.7/\text{rev}$) to soft inplane ($\omega_\zeta/\Omega \sim 0.7/\text{rev}$). For

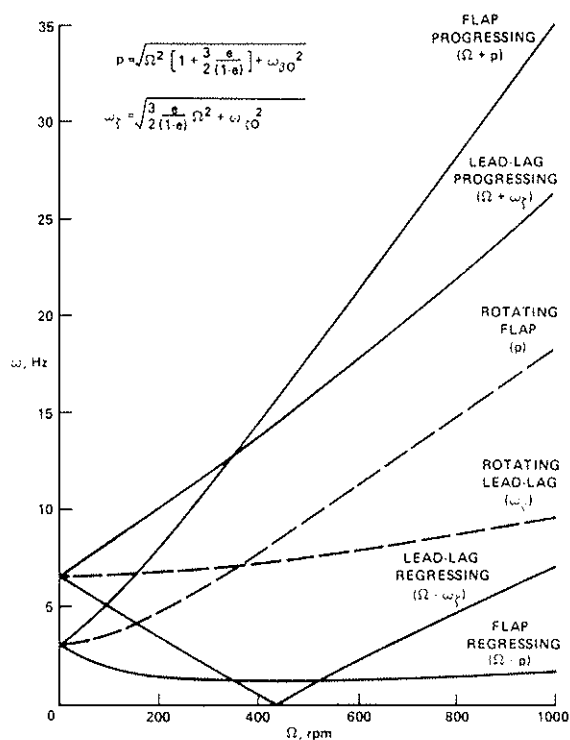


Fig. 8. Uncoupled rotor frequencies in rotating and fixed systems.

specific configurations, secondary parameter variations were included, such as body stiffness (frequency) and blade pitch angle, but these variations were not extensive.

The experimental model properties required for use in the theoretical model were obtained from nonrotating measurements. The body spring stiffnesses in the simulated vacuum case, for instance, were calculated based on the measured nonrotating body frequencies, using the uncoupled pitch and roll equations, and assuming the blade motion was locked out due to the restraint of the blade droop stops. The bending and torsional stiffness of the single element flexbeam of the theoretical model were determined directly from measurements of blade nonrotating frequencies. No adjustments were made to any of these properties to improve the correlation between the theory and

experimental data. The input properties used by the theoretical model are described in Ref. 14. An exception to the above comments was the specification of body damping. Estimates of the nonlinear gimbal damping from nonrotating tests necessarily represent some sort of "average" damping, which may or may not provide a good approximation of the nonlinear effects. Rather than using such an average, the body damping was arbitrarily set to 3% of critical, and the effect of this assumption was examined by calculating results at half and double this value.

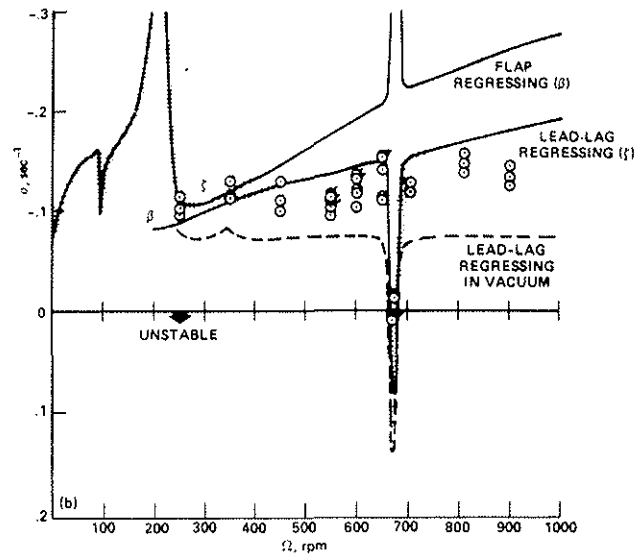
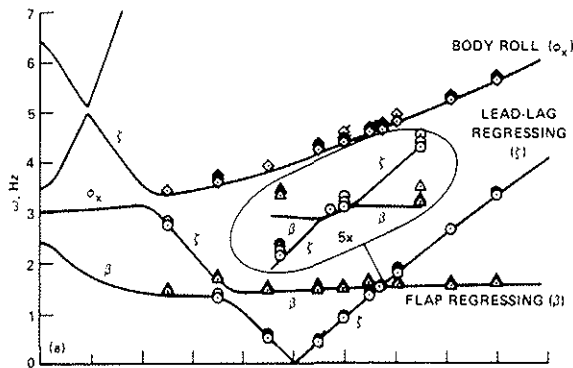


Fig. 9. Tantalum stub blades with roll freedom. $\omega_{\phi_x} = 2.60$ Hz (flagged symbols are $\omega_{\phi_x} = 2.56$ Hz; shaded area shows effect of halving and doubling nominal body damping). (a) Modal frequencies. (b) Lead-lag regressing mode damping.

8.1 Tantalum Stub Blades with Roll Freedom

The tantalum stub blades were run with just the body roll degree of freedom by locking out the pitch motion of the gimbal frame. This resulted in the model and stand having a first pitch frequency of approximately 27 Hz, which is well separated from the body roll and rotor regressing mode frequencies. By testing with the tantalum stub blades to simulate a vacuum and locking out the body pitch degree of freedom, it was possible to examine an extremely simple coupled rotor-body system. The theory is compared with the experimental results in Fig. 9 for the case of a nonrotating body frequency of 2.60 Hz.

The plot of modal frequencies shows the rotor regressing and body mode frequencies (and a small portion of the flap progressing mode) as a function of rotor speed.

The experimental estimates of lead-lag regressing mode frequency were obtained from the ζ_c cyclic coordinate, following excitation of the lead-lag regressing mode, and are indicated by circles. The body roll and flap regressing mode frequency measurements were obtained from the roll axis potentiometer, following the deflection and release of the model in roll, and are indicated by diamonds for the body roll mode and triangles for the flap regressing mode. Because these modes comprise more than one degree of freedom, the names "body roll" or "flap regressing" are only a convenient means of naming the modes, but do not constitute an exact description.

As rotor speed increases, the lead-lag mode decreases in frequency until resonance with the rotor speed is reached at about 505 rpm. Above this resonance, the lead-lag regressing mode increases with increasing rotor speed. The body roll mode is also rotor-speed dependent within the range of rotor speeds tested and increases quickly enough with rotor speed to prevent any coalescence with the lead-lag regressing mode. Interestingly enough, the flap regressing mode coalesces with the lead-lag regressing mode at about 670 rpm, and a very weak mechanical instability occurs. This coalescence is shown scaled up five times in the inset to the figure. This weak instability is discussed in Ref. 7 and is limited to rotors in a vacuum or, as in this case, in a simulated vacuum. The correlation between the theory and experiment for modal frequency is excellent. Even at the expanded scale of the inset, the correlation is still quite good.

Figure 9(b) shows the lead-lag regressing mode damping as a function of rotor speed. Although attempts were made to estimate the damping of the body roll and flap regressing modes, the nonlinearity in the gimbal ball bearings was evident in both modes, and no suitable quantitative estimates could be made. Despite the nonlinear gimbal damping, however, the lead-lag regressing mode damping was linear and well-behaved, except for a few configurations in the vicinity of stability boundaries (these points are noted when they occur). The experimental damping measurements show considerably more scatter than in the measurements for frequency, and clearly show the weak instability at the coalescence of the flap and lead-lag regressing modes. The theoretical prediction of lead-lag regressing mode damping shows good agreement with the data, except for an overestimation of the damping level, particularly at higher rotor speeds. Although the nonlinear character of the gimbal bearing damping cannot be included in the theoretical model, the effect of different levels of body damping may be used to examine the sensitivity of the predicted results to body damping. The shaded areas in this figure show the effect of halving and doubling the nominal body damping of 3%. For the most part, the lead-lag regressing mode is insensitive to the amount of body damping, except when the flap and lead-lag regressing mode frequencies are proximate. This suggests that the experimental measurements of lead-lag regressing mode damping are valid, despite the nonlinear gimbal damping. In addition, it does not appear that the difference in damping level between theory and experiment can be ascribed to the nonlinear gimbal damping. The computed modal frequencies are not affected by the level of gimbal damping.

The lead-lag regressing mode damping calculated for an actual vacuum is also shown in this figure, and it can be seen that these predictions are significantly less than the simulated vacuum predictions, a difference due to the profile drag damping of the tantalum stub blades ($c_{d_0} = 1.0$). The original purpose in doing simulated vacuum tests was to examine the effects of inertial and structural terms without the influence of blade aerodynamics. Although the effects of residual aerodynamics on the lead-lag regressing mode damping are significant, the character of the true vacuum behavior is retained in the simulated vacuum case.

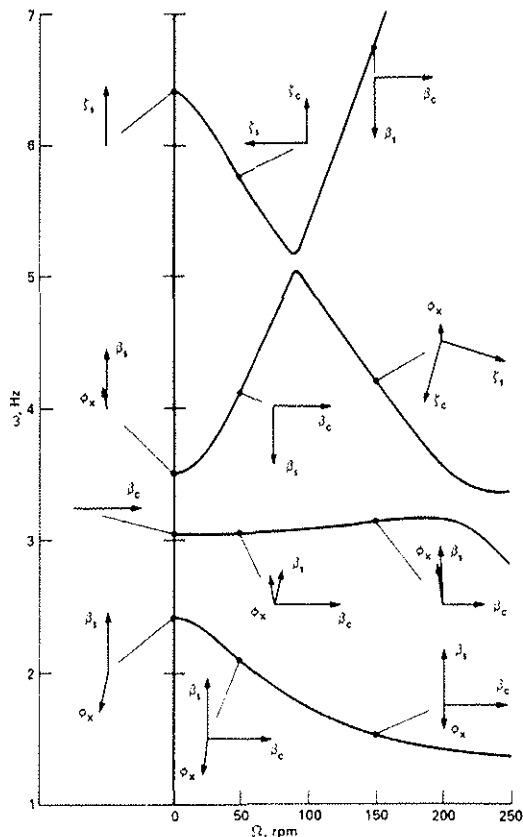


Fig. 10. Mode shapes for tantalum stub blades with roll freedom (modal frequency from Fig. 9).

been given to it. The next higher mode in frequency, at zero rotor speed, shows purely cosine flapping. In this case, the rotor disk is tilting back and forth about the pitch axis, its motion reacted by the infinite stiffness of the body pitch coordinate. The third mode at zero rpm consists of sine flapping and body roll as in the first case, but now the motions are out of phase (inphase vectors mean out-of-phase motion due to the sign convention). This kind of motion, where the rotor disk tilts one way and the body tilts the other, is analogous to the second bending mode of a beam. If rotor speed is increased to 50 rpm, this third mode changes character and becomes purely a flapping mode (the flap progressing mode), while the characteristic of out-of-phase sine flapping and body roll motion now becomes the property of the second mode, a mode previously referred to as the "body roll" mode. It is now possible to see that the body roll and flap-regressing modes both have significant amounts of body and flapping motion in them and that they are distinguished by the phasing of the motions. The flap regressing mode is where the rotor disk tilts with the body and has the lower frequency. The body roll mode is where the disk tilts in opposition to the body and has the higher frequency.

The fourth mode in Fig. 10 shows sine lead-lag motion at zero rpm. This mode is the lead-lag oscillation of the blades against the restraint of the locked-out pitch degree of freedom. As rotor speed is increased to 50 rpm, the mode is made up of sine and cosine lead-lag motion. At higher rotor speeds this mode takes on the character of pure flapping oscillations, that is, the flap progressing mode, while the third mode, that was previously

The behavior of the coupled rotor-body modes is more readily understandable if the mode shapes are examined. The modal frequency plot of Fig. 9(a) from zero to 250 rpm is expanded in Fig. 10, and the calculated mode shapes for selected rotor speeds are plotted on the figure. For each mode a vector is used for each coordinate to show relative amplitude and phase. The cosine flap coordinate, β_c , has been selected as a zero phase reference. If the lowest frequency mode at zero rotor speed is examined, it can be seen that it consists of sine flapping, β_s , and body roll. Because of the sign convention used here, inphase motion of β_s and ϕ_x is represented by vectors of opposite phase, and vice versa. Thus, the motion of this mode shape is the body and rotor moving together in a fashion analogous to first-mode bending of a beam. As the rotor speed is increased from zero, this motion persists with the addition of cosine flapping. From the mode shapes of this first mode, it is clear that this is a combined body-flapping mode, despite the name "flap regressing" that has

discussed, now shows mostly lead-lag oscillations and has become the lead-lag regressing mode.

From a mathematical point of view, the various modes are unique and well defined. For instance, the third mode in Fig. 9(a) starts out with primarily sine and cosine flapping (flap progressing), the mode shape changes as rotor speed is increased, and the character becomes sine and cosine lead-lag oscillations (lead-lag regressing). Above 250 rpm the mode takes on the behavior of out-of-phase roll and sine flapping motions (body roll). Despite the different behavior this mode shows at different rotor speeds, it is a single, unique mode, as would be clearly seen if it had been shown on a root locus plot. But, to understand the behavior of the system from a physical point of view, it is necessary to consider the physical modal behavior. Thus, the lead-lag regressing "mode" starts out as the fourth mode, but as rotor speed is increased it becomes, progressively, the third, second, and finally, the first mode. An element of confusion is probably inherent in the process of referring to separate mathematical modes as a single physical "mode," but the process is essential to understanding the system behavior.

An additional case was run with the tantalum stub blades and roll freedom alone, which included excitation of the lead-lag progressing mode as well as the lead-lag regressing mode. The nonrotating body roll frequency was lowered to 1.89 Hz for this case, and the theory and experiment are compared in Fig. 11. The behavior of the rotor regressing and the body roll modes is similar to that shown in Fig. 9. The agreement between the theory and experiment for modal frequency is again excellent, while the agreement is good for lead-lag regressing damping. Lead-lag progressing mode frequency and damping were obtained by oscillating the model in roll at the progressing mode frequency and estimating the frequency and damping from the transient decay. These data are shown in the figure as solid diamonds. A fifth mode is added to the collection described previously. This mode starts out as the lead-lag progressing mode, and in the vicinity of 400 rpm the mode becomes the flap progressing mode. The fourth mode, which is the flap progressing mode below 400 rpm, turns into the lead-lag progressing mode. The agreement between the predicted lead-lag progressing frequency and the measurements is very good below 400 rpm but is degraded at higher rotor speeds. Similarly, the prediction of modal damping is good below 400 rpm, but at higher rotor speeds the damping is significantly underpredicted.

If the pitch degree of freedom is added to the analysis, and the nonrotating measurement of pitch frequency is used to specify the pitch stiffness, then the agreement between theory and experiment is much improved, as shown by the dashed lines in Fig. 11. The theoretical prediction of the lead-lag progressing mode frequency now shows the same trend as the data, although the agreement is not as good as for the low-frequency modes. The agreement between theory and experiment for the modal damping is not as good as in the frequency case, but it seems clear that the pitch degree of freedom is responsible for the rapid rise in damping that is seen for rotor speeds above 400 rpm. Unlike for the lead-lag regressing mode, the lead-lag progressing mode damping is very sensitive to the amount of damping in the roll gimbal bearings, and this may be responsible for some of the difference between theory and experiment in Fig. 11(b). It is noted that the theoretical predictions for the body roll and rotor regressing mode damping and frequency are the same whether the pitch degree of freedom is included or not. This demonstrates that

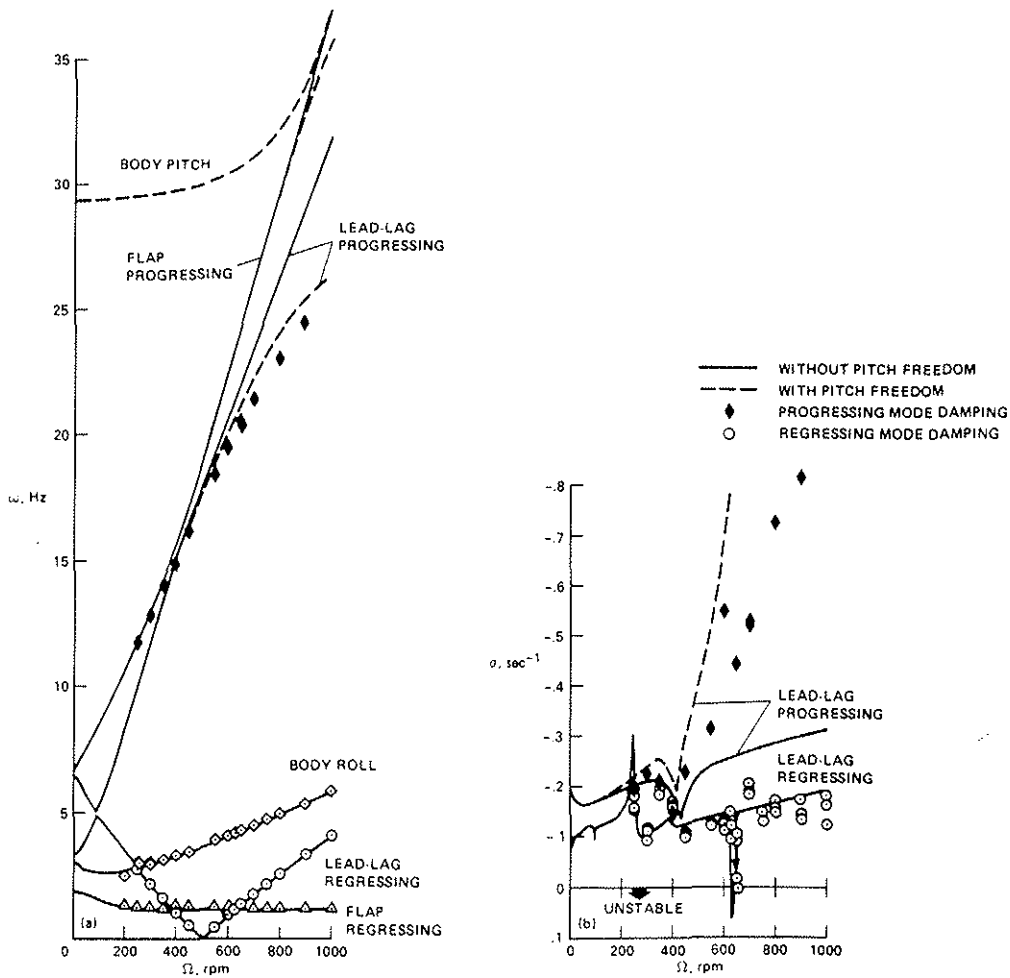


Fig. 11. Tantalum stub blades with roll freedom including progressing modes; $\omega_{\phi_X} = 1.89$ Hz. (a) Modal frequencies. (b) Lead-lag mode damping.

tests with a single body degree of freedom can be successfully performed if the frequency of the extra body mode is placed sufficiently far away from the frequency of the modes of interest.

8.2 Tantalum Stub Blades with Pitch and Roll Freedom

The model was tested with the tantalum stub blades, and with both pitch and roll freedom. The nonrotating pitch and roll frequencies were selected to have approximately the same value. A comparison of theory and experiment for modal frequency and damping is shown in Fig. 12.

The major change that results with the addition of the body pitch mode is that the lead-lag regressing and body pitch modes coalesce, and a severe mechanical instability of the ground resonance type occurs at about 860 rpm. Interestingly enough, the weak instability and frequency coalescence between the flap and lead-lag regressing modes, which was seen in the roll freedom alone configuration, is now absent. The correlation between theory and experiment for modal frequency is quite good, although it appears from the experimental data that the body pitch frequency approaches coalescence with the lead-lag regressing mode frequency at lower rotor speeds than predicted by theory.

The nonlinear damping in the gimbal bearings causes estimates of flap regressing or body mode damping to be unsuitable, as in the roll freedom alone case. The lead-lag regressing mode damping for the most part is insensitive to the level of body damping over the rotor speed range tested, except in the vicinity of 400 rpm, where the flap and lead-lag regressing modes are strongly coupled, and near the stability boundary. In the vicinity of the stability boundary a number of test points show apparent nonlinearities. These are indicated in the figure by an arrow that extends from the initial damping level to the final damping level measured at the end of a data record. The nonlinearity in damping in this case is in the same sense as the gimbal bearing damping, that is, the damping decreases as amplitude increases. In general, the agreement between theory and experiment for the lead-lag regressing mode damping is good. The data scatter is reduced from the roll freedom alone case, but the reduction is exaggerated by the condensation of the ordinate scale.

The addition of the body pitch mode complicates the behavior of the various modes. The flap regressing mode is essentially as before: it is made up of the disk tilting in the same direction as the body tilt, and the two travel together around the azimuth at the flap regressing mode frequency. The body pitch and roll modes both represent out-of-phase motion, with the body tilting in the opposite direction from the rotor disk. The major difference between the two modes is that the pitch mode shows relatively more body deflection than flapping deflection, while the roll mode shows more flapping deflection than body deflection. Both body modes have considerable pitch and roll motion in them, although the pitch mode has more pitch deflection than roll deflection, and the roll mode has more roll deflection than pitch deflection.

8.3 Aerodynamic Blades with Pitch and Roll Freedom

The model was tested with the aerodynamic blades installed at blade pitch angles of 0° and 8.9° . The same body springs were used for the pitch and roll axes as for the tantalum stub blade case, but because of the reduced rotor mass there was an increase in the nonrotating body frequencies from 2.58 to 2.62 Hz for pitch, and 2.55 to 2.75 Hz for roll. The first blade pitch angle case is representative of a ground resonance condition as there

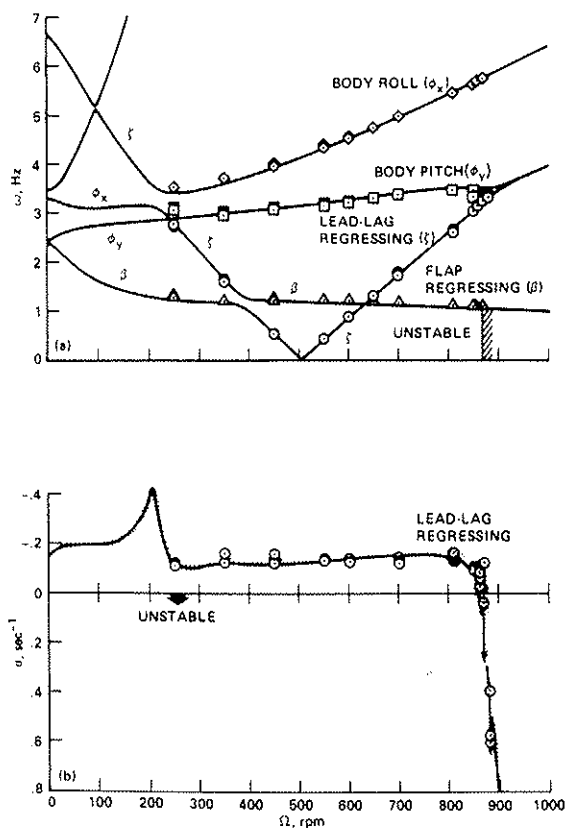


Fig. 12. Tantalum stub blades with pitch and roll freedom; $\omega_{\phi_x} = 2.55$ Hz, $\omega_{\phi_y} = 2.58$ Hz (shaded area shows effect of halving and doubling nominal body damping). (a) Modal frequencies. (b) Lead-lag regressing mode damping.

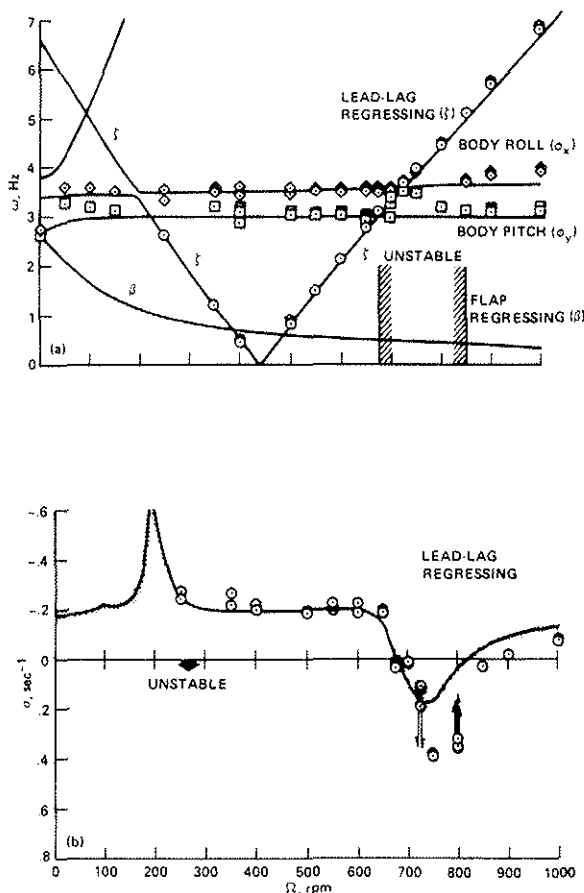


Fig. 13. Aerodynamic blades with pitch and roll freedom; $\omega_{\phi_x} = 2.73$ Hz, $\omega_{\phi_y} = 2.62$ Hz, $\theta_b = 0^\circ$. (Shaded area shows effect of halving and doubling nominal body damping.) (a) Modal frequencies. (b) Lead-lag regressing mode damping.

range where the system is unstable, significant differences appear between the calculated and measured body frequencies, but this may be due to the difficulty in making accurate measurements of the frequency of a stable mode in the presence of an unstable one. Overall, the correlation for the modal frequencies is good.

The theoretical calculation of lead-lag regressing mode damping shows good agreement with the data at rotor speeds up to the lower stability boundary. Beyond this point the theory underestimates the amount of unstable damping, and as rotor speed is increased the theory overpredicts the recovery in damping. Although the theory shows that the lead-lag damping is sensitive to the level of body damping in the unstable rotor speed range and beyond, this is not enough to explain the observed differences. The theoretical model uses a symmetrical airfoil, and so for these conditions there is no inflow. The experimental model, however, employs a cambered airfoil and in this respect fails to match the theory. The inexact match between theory and experiment results in an ambiguity—it is not known how much of the difference can be explained by the effects of camber and inflow. As in the tantalum stub

is very little thrust on the rotor (there is some thrust due to blade camber). The modal frequencies and lead-lag regressing mode damping for this condition are shown in Fig. 13.

The modal frequencies in this case illustrate a number of differences with the comparable tantalum stub blade configuration. Because the hinge offset is significantly reduced, the lead-lag regressing mode frequency varies more rapidly with rotor speed than before. The flap regressing mode is now heavily damped by the blade aerodynamics, and frequency information could not be obtained with transient excitation techniques. The body pitch and roll mode frequencies are virtually independent of rotor speed, and cross the lead-lag regressing mode rather than coalescing with it. The lead-lag regressing mode is unstable over a fairly wide range in rotor speed, but the instability is considerably milder than in the tantalum blade case. This tendency of aerodynamics to reduce the severity of the instability as compared to the vacuum case is noted in Ref. 7. The correlation between the theoretical predictions of frequency and the measurements is not as good as for the simulated vacuum conditions. The body mode frequencies show slight areas of disagreement, at both high and low rotor speeds. The lead-lag regressing mode frequency shows a systematic difference that is greatest at the maximum rotor speed and may reflect the effect of the model blade flexibility. In the rotor speed

blade configuration, there are experimental measurements that show apparent nonlinearities in damping in the unstable regime. The test points at 725 rpm show damping variation with amplitude that has the same sense as the gimbal bearings, that is, as amplitude increases, the damping becomes less. What is more interesting is that at 800 rpm the nonlinear damping is opposite to the sense seen in the gimbal bearings. The reason for these nonlinearities is unknown.

The mode shapes in the aerodynamic case are not significantly different from the tantalum stub blade case. Perhaps most interesting is how the various flapping-body modes are affected by the increase in aerodynamic flap damping. The flap regressing mode has become heavily damped, and this seems reasonable as the mode is made up of inphase flapping and body motions. Thus, tilt of the disk is accentuated by tilt of the body, and the normal flapping velocity is increased by the body rotation. For the body modes the rotor disk motion is opposite in phase to the body motion, and the effect of the flap damping is significantly reduced. In effect the flapping velocity is decreased by the opposite motion of the body. It is these body modes that couple with the lead-lag regressing mode to cause aeromechanical instabilities of the air and ground resonance type. The fact that the body motions are out of phase with blade flapping may explain why techniques that are effective in augmenting lead-lag damping for rigid hub conditions lose all effectiveness when body freedom is added (Ref. 16).

The theory is compared with the experiment for the high thrust case where $\theta_b = 8.9^\circ$ in Fig. 14. Experimental measurements were made for rotor speeds at 550 rpm and above. The modal frequencies are similar to the low thrust case, and the same systematic difference between theory and experiment is seen for the lead-lag regressing mode. The calculated values for body roll mode frequency are less than the measured values, but in general, the correlation is good.

The lead-lag regressing mode damping is considerably changed from the low thrust case. The effect of blade pitch angle and thrust is to significantly increase the damping at rotor speeds below the stability boundary, and to increase the size and the severity of the unstable region (Ref. 7). The theory shows reasonable agreement with the data, and in particular calculates the amount of unstable damping quite well. However, it underestimates the recovery in the damping at the upper stability boundary, a trend that is opposite to that seen in

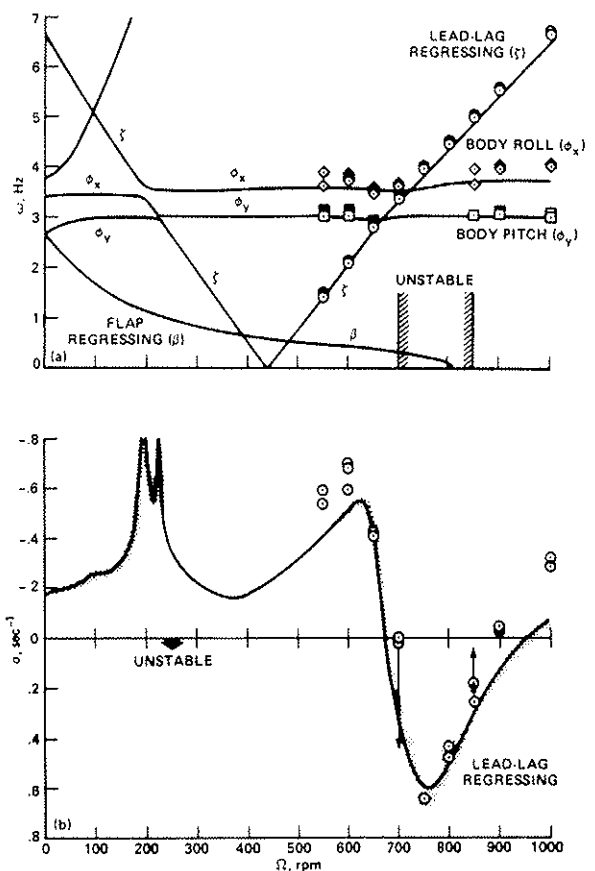


Fig. 14. Aerodynamic blades with pitch and roll freedom; $\omega_{\phi_x} = 2.73$ Hz, $\omega_{\phi_y} = 2.62$ Hz, $\theta_b = 8.9^\circ$. (Shaded area shows effect of halving and doubling nominal body damping.) (a) Modal frequencies. (b) Lead-lag regressing mode damping.

the low thrust case. Apparent nonlinearities in damping again appear in the unstable region, and as in the low thrust case, the sense of the nonlinearity is the same as the gimbal bearing nonlinearity at the lower speed and opposite in sense at the higher speed.

9. Concluding Remarks

The experiment reported in this paper was undertaken to obtain data for the validation of simplified theoretical models of coupled rotor-body systems, and to obtain a better understanding of hingeless rotor helicopter aeromechanical stability. The following conclusions are offered:

(1) Modal frequency data of excellent quality were obtained for the lead-lag regressing mode, the body pitch and roll modes, and in the simulated vacuum case for the flap regressing mode. Modal damping data for the lead-lag regressing mode were also obtained and were of good quality.

(2) Nonlinear damping characteristics of the gimbal ball bearing prevented acquiring adequate modal damping data for the flap regressing or body modes. No significant effect on the modal frequency measurements or lead-lag regressing mode damping due to the gimbal damping was observed.

(3) Both theory and experiment show a weak mechanical instability to occur when the flap and lead-lag regressing mode frequencies coalesce under simulated vacuum conditions and with roll freedom alone. This instability was predicted in Ref. 7.

(4) Both theory and experiment demonstrate a mechanical instability of the ground resonance type for the simulated vacuum tests with pitch and roll freedom.

(5) Both theory and experiment show aeromechanical instabilities for tests with the aerodynamic blades installed with pitch and roll freedom. Aeromechanical instability occurs at both low and high thrust conditions.

(6) The correlation between theory and experiment for modal frequency is in general very good. The correlation for lead-lag regressing mode damping is generally good. Agreement between experiment and theory is better for the simulated vacuum tests than with the aerodynamic blades installed.

(7) The use of circular cross-section blades of tantalum to simulate vacuum testing is a useful technique. Despite some residual effects due to profile drag, the tantalum stub blades used in the experiment provide a good approximation of the behavior of a coupled rotor-body system in a vacuum.

(8) The progression in test configurations from simulated vacuum with only one body degree of freedom, to an aerodynamic blade configuration with both pitch and roll freedom, provided an opportunity to observe the fundamental behavior of coupled rotor-body systems as complexity was increased.

(9) Calculation of mode shapes provided basic knowledge of the behavior of the model. The flap regressing and body modes all contain substantial flapping and body motion. The flap regressing mode is distinguished from the body modes by the inphase tilting of the disk with the body (like the first bending mode of a beam). With the inclusion of aerodynamics this mode is highly stabilized. The body modes are characterized by out-of-phase

motion of the rotor disk and body, and these are the modes that couple with the lead-lag regressing mode for ground and air resonance. With the addition of aerodynamics these modes are not strongly damped.

(10) The stringent requirements that were established for experimental data to be used in the validation of theoretical models were not entirely met. With respect to the match between the theory and the experimental model, the nonlinear gimbal damping, and aerodynamic blade flexibility and camber leave some ambiguity as to the cause of differences seen between theory and experiment. The nonlinear bearing damping prevented satisfactory measurements of the body modal damping, and this decreased the number of bases of comparison for theory and experiment. Lastly, more parameter variation is required, particularly to examine the effects of blade pitch angle variation.

REFERENCES

1. Robert P. Coleman and Arnold M. Feingold, Theory of Self-Excited Mechanical Oscillations of Helicopter Rotors with Hinged Blades, NACA TR-1351, 1958.
2. R. T. Lytwyn, W. Miao, and W. Woitsch, Airborne and Ground Resonance of Hingeless Rotors, Journal of the American Helicopter Society, Vol. 16, No. 2, April 1971, pp. 2-9.
3. R. E. Donham, S. V. Cardinale, and I. B. Sachs, Ground and Air Resonance Characteristics of a Soft Inplane Rigid Rotor System, Journal of the American Helicopter Society, Vol. 14, No. 4, October 1969, pp. 33-41.
4. J. C. A. Baldock, Some Calculations for Air Resonance of a Helicopter with Non-articulated Rotor Blades, RAE Technical Report 72083, August 1972.
5. John E. Burkham and Wen-Liu Miao, Exploration of Aeroelastic Stability Boundaries with a Soft-In-Plane Hingeless Rotor Model, Journal of the American Helicopter Society, Vol. 17, No. 4, October 1972, pp. 27-35.
6. Wen-Liu Miao and Helmut B. Huber, Rotor Aeroelasticity Coupled with Helicopter Body Motion, NASA SP-352, February 1974, pp. 137-146.
7. Robert A. Ormiston, Aeromechanical Stability of Soft Inplane Hingeless Rotor Helicopters, Proceedings of the Third European Rotorcraft and Powered Lift Aircraft Forum, Paper No. 25, September 1977.
8. Robert A. Ormiston, Helicopter Modelling, The Aeronautical Journal, Vol. 77, No. 755, November 1973, pp. 579-591.
9. Dewey H. Hodges, A Theoretical Technique for Analyzing Aeroelastic Stability of Bearingless Rotors, Proceedings of the 19th AIAA/ASME Structures, Structural Dynamics and Materials Conference, April 1978, pp. 282-294.
10. Dewey H. Hodges, Aeromechanical Stability of Helicopters with a Bearingless Main Rotor - Part I: Equations of Motion, NASA TM 78459, February 1978.
11. Kurt H. Hohenemser and Sheng-Kuang Yin, Some Applications of the Method of Multiblade Coordinates, Journal of the American Helicopter Society, Vol. 17, No. 3, July 1972, pp. 3-12.

12. W. G. Bousman, D. L. Sharpe, and R. A. Ormiston, An Experimental Study of Techniques for Increasing the Lead-Lag Damping of Soft Inplane Hingeless Rotors, 32nd Annual National V/STOL Forum of the American Helicopter Society, Preprint No. 1035, May 1976.
13. Leonard Meirovitch, Elements of Vibration Analysis, McGraw-Hill, Inc., 1975, pp. 21-24.
14. William G. Bousman, An Experimental Investigation of Hingeless Helicopter Rotor-Body Stability in Hover, NASA TM 78489, June 1978.
15. William G. Bousman, An Analog Technique for the Measurement of Damping from Transient Decay Signals, NASA TM X-73,121, June 1976.
16. Robert A. Ormiston, Concepts for Improving Hingeless Rotor Stability, Proceedings of the American Helicopter Society Mideast Region Symposium on Rotor Technology, August 1976.

NOTATION

a	lift curve slope
b	number of blades
c	blade chord, m
c_{d0}	blade profile drag coefficient
e	dimensionless offset of hinge from rotor center
\mathcal{F}	function to be minimized to produce rotor equilibrium solution
[F]	flexbeam flexibility matrix
F	steady component of F_k, N
F_k	force acting on the kth blade, N
\tilde{F}_k	perturbation oscillatory component of F_k, N
F_R	force at the flexbeam root, made dimensionless by $\frac{I\Omega_0^2}{\ell}$
$\tilde{F}_{u_k}, \tilde{F}_{v_k}, \tilde{F}_{w_k}$	perturbation components of force in the direction of u,v,w, respectively, acting at the flexbeam tip
h	height of rotor-hub center above aircraft reference center, m
I	rotor blade flapping inertia about flexbeam tip, $\text{kg}\cdot\text{m}^2$
I_x, I_y	body mass moment of inertia for the body mass center for axes N_A and N_B , respectively, $\text{kg}\cdot\text{m}^2$
L	blade length, m
ℓ	flexbeam length, m

M	steady component of M_k , N-m
M_k	moments exerted on the kth blade, N-m
\tilde{M}_k	perturbation oscillatory component of M_k , N-m
M_R	moment at the flexbeam root, made dimensionless by $I\Omega_0^2$
$\tilde{M}_{\zeta k}, \tilde{M}_{\beta k}, \tilde{M}_{\theta k}$	perturbation components of moments in the direction of ζ, β, θ , respectively, acting at the flexbeam tip
m	mass of one rotor blade, kg
m_f	mass of the fuselage, kg
N_A, N_B, N_C	body-fixed coordinate system, Fig. 1
N_1^k, N_2^k, N_3^k	coordinate system that rotates at angular velocity Ω , Fig. 1
n_1^k, n_2^k, n_3^k	coordinate system fixed in the kth undeformed flexbeam
n_x^k, n_y^k, n_z^k	coordinate system fixed in the kth deformed flexbeam tip
p	dimensionless blade flapping frequency, Fig. 8
R	rotor radius, m
u	steady component of u_k , m
u_k	axial deflection of the kth flexbeam tip, m
v	steady component of v_k , m
v_k	chordwise deflection of kth flexbeam tip, m
w	steady component of w_k , m
w_k	flapwise deflection of kth flexbeam tip, m
{x}	column vector with elements: $\tilde{u}_c, \tilde{u}_s, \tilde{v}_c, \tilde{v}_s, \tilde{w}_c, \tilde{w}_s, \tilde{\zeta}_c, \tilde{\zeta}_s, \tilde{\beta}_c, \tilde{\beta}_s, \tilde{\theta}_c, \tilde{\theta}_s, \phi_x, \phi_y$
z	vertical distance from aircraft reference center to body mass center, positive when body mass center is below reference center, m
β	steady component of β_k , rad
β_c	cosine flap coordinate, rad
β_k	elastic flap rotation of the kth flexbeam tip, positive tip up, rad
β_s	sine flap coordinate, rad
γ_d	modified Lock number, Eq. (9)

ϵ	perturbation of flexbeam tip loads
ζ	steady component of ζ_k , rad
ζ_c	cosine lead-lag coordinate, rad
ζ_k	elastic lead angle of the k th flexbeam tip, positive tip leading, rad
ζ_{LOCAL}	local damping ratio, Fig. 6, percent critical
ζ_s	sine lead-lag coordinate, rad
θ	steady component of θ_k , rad
θ_b	built-in pitch angle of the blade with respect to the flexbeam, positive leading edge up, rad
θ_i	local deflection angle, Fig. 6, deg
θ_k	elastic twist of the k th flexbeam tip, positive leading edge up, rad
ρ	air density, kg/m^3
ρ_d	density of circular cross-section blades, kg/m^3
σ	damping exponent, sec^{-1}
ϕ_x	time integral of angular velocity component in N_A direction, rad
ϕ_y	time integral of angular velocity component in N_B direction, rad
ψ_k	azimuth angle of k th blade = $\Omega t + 2\pi(k-1)/b$
Ω	rotor angular velocity, rad/sec, Hz, or rev/min
Ω_0	nominal rotor angular velocity, rad/sec
ω	modal frequency, Hz
ω_ζ	frequency of lead-lag motion, Hz
$\omega_{\zeta_0}, \omega_{\beta_0}$	frequency of lead-lag, flapwise motion, respectively when $\Omega = 0$, Hz
$\omega_{\phi_x}, \omega_{\phi_y}$	frequency of body roll, pitch motion, respectively when $\Omega = 0$, Hz

Flexbeam tip deflection notation (x represents deflections u, v, w, β , ζ , θ):

$$\tilde{x}_c \quad \frac{2}{b} \sum_{k=1}^b \tilde{x}_k \cos \psi_k$$

\tilde{x}_k unsteady component of x_k

$$x_s \quad \frac{2}{b} \sum_{k=1}^b \tilde{x}_k \sin \psi_k$$

x_t assumed value for x in equilibrium deflection scheme, made dimensionless by l for u, v, and w